Room-temperature phosphorescence in crystalline bifurcating halogen···halogen synthon containing chromophore

Suvarna Sujilkumar, Agaja Kalyani and Mahesh Hariharan*

School of Chemistry, Indian Institute of Science Education and Research Thiruvananthapuram, Vithura, Thiruvananthapuram, Kerala, India 695551

Supporting Information (SI)

Contents

Section A: Materials and Methods 3-7

1.1 X-ray Crystallography 3

1.2 Computational Details 4

1.3 Noncovalent interaction (NCI) Plot 4

1.4 Hirshfeld Analysis 4

1.5 Energy Framework Analysis 4

1.6 Quantum Theory of Atoms in Molecules (QTAIM) 5

1.7 Symmetry Adapted Perturbation Theory (SAPT) 5

1.8 Excitonic Coupling Parameters 5

1.9 Anisotropic Charge Transport Mobility 6

2.0 TheoDORE Analysis 7

2.1 Electrostatic Potential Map 7

Section B: Synthesis and Characterization 8

Scheme S1: Shows the synthesis of Pentacenedione and P-Br_4. 8

Section C: Tables 9-13

Table S1: Crystallographic data and refinement parameters for P-Br_4. 9

Table S2: Interaction energies in selected dimers determined by SAPT(0)/aug-cc-Pvdz calculations and SAPT(0) energy components for P-Br_4 10

Table S3: Relative % intermolecular interactions obtained from Hirshfeld analysis 10

Table S4: Intermolecular interaction energies of molecular pairs in P-Br_4 calculated using energy framework analysis 11

Table S5: Calculated topological properties of electron density function for the intermolecular interactions forming bifurcating synthons in PBr_4 12

Table S6: Computed long-range Coulombic ($J_{Coulomb}$) and short-range charge transfer integral (t_e and t_h) for the dimers of P-Br_4 12

Table S7: Mean position (POS), participation ratio (P_R), charge transfer character (CT), and exciton character of excited states in P-Br_4 12

Table S8: Vertical excitation energy of CAM-B3LYP/def2svp-Optimized geometry of PBr_4 13

Table S9: Spin-orbit coupling values between the singlet and triplet states of P-Br_4 13

Section D: Figures 14-23

Fig. S1: ^{1}H NMR spectrum of P-Br_4 in $CDCl_3$. 14

Fig. S2: ^{13}C NMR spectrum of P-Br_4 in $CDCl_3$ 14

Fig. S3: ^{1}H NMR spectrum of Pentacene-6,13-dione in $CDCl_3$. 15

Fig. S4: HRMS spectrum of P-Br_4. 16

Fig. S5: HRMS spectrum of Pentacene-6,13-dione 17

Fig. S6: Crystal packing of P-Br_4 viewed along a) a, b) b, and c) c axis, respectively**.** 17

Fig. S7: a) Image of the PBr_4 crystal under daylight, b) UV excitation, and c) after removal of the UV light. 18

Fig. S8: A bifurcating synthon formed through Br···Br interactions with distance ($d_{Br\cdots Br}$) ranging from 3.141 Å to 3.766 Å..... 18

Fig. S9: a) Dimer-1 b) Dimer-2 and c) Dimer-3 with centroid to centroid distance 18

Fig. S10: NCI analysis of P-Br_4 dimer. 19

Fig. S11: Hirshfeld 2D fingerprint plots a) Total, b) C•••Br, c) C•••H, (d) H•••Br e) H•••H and f) Br•••Br interactions of crystalline P-Br_4. 19

Fig. S12: Energy frameworks calculated for P-Br_4 crystal a) coulombic component (red), b) dispersion component (green), and c) total energy (blue). 20

Fig. S13: QTAIM topological plot of P-Br_4 dimer where the small yellow circles indicate bond critical points and large circles correspond to atomic nuclei (C, H, and Br). The yellow lines represent bond paths. 20

Fig. S14: QTAIM topological plot of P-Br_4 dimer where the small yellow circles indicate bond critical points and large circles correspond to atomic nuclei (C, H, and Br)..... 21

Fig. S15: QTAIM topological plots of P-Br_4 dimer2 and dimer3 where the small yellow circles indicate critical points and large circles correspond to atomic nuclei (C, H, and Br). The yellow lines represent bond paths..... 21

Fig. S16: Electrostatic surface potential (ESP) plot of P-Br_4..... 21

Fig. S17: a) Electron-hole correlation plots of excited states of P-Br_4. and b) Fragments used for analysis..... 22

Fig. S18: (a) Anisotropic hole (μ_h, blue) and electron (μ_e, violet) mobility for P-Br_4 and (b) representation of conducting channel. 22

Fig. S19: a) UV-VIS absorption and b) emission spectra of P-Br_4 in THF solution..... 22

Fig. S20: Kubelka-Munk transformed diffuse reflectance spectrum of P-Br_4 crystals..... 23

Fig. S21: Room temperature phosphorescence decay of P-Br_4 crystal..... 23

Fig. S22: a) Room temperature and 77 K phosphorescence spectra and b) 77 K phosphorescence decay of P-Br_4 crystal..... 23

Coordinates 24

References..... 24-25

Section A: Materials and Methods

All chemicals were obtained from commercial suppliers and used as received without further purification. All reactions were carried out in oven-dried glassware before use and wherever necessary, were performed under dry nitrogen in dried, anhydrous solvents using standard gastight syringes, cannula, and septa. Solvents were dried and distilled by standard laboratory purification techniques. TLC analysis was performed on silica gel 60 F254 plates (0.25 mm, Merck), and developed TLC plates were visualized under short and long-wavelength UV lamps. Column chromatography was performed using silica gel of 200-400 mesh employing a solvent polarity correlated with the TLC mobility observed for the substance of interest. Yields refer to chromatographically and spectroscopically homogenous substances. ^{1}H NMR spectra were measured on a 500 MHz Bruker Avance DPX spectrometer. The internal standard used for ^{1}H NMR is tetramethyl silane (TMS). High-resolution mass spectra (HRMS) were recorded on Thermo Scientific Q Exactive mass spectrometer using electrospray ionization (APSI, positive mode) technique.

Photoluminescence Measurements: Absorption and emission spectra were recorded on UV-Vis-NIR Perkin Elmer Lambda 950 spectrometer. Emission measurements were carried out using the Horiba Jobin Yvon Fluorolog spectrometer. Photophysical measurements in the solution state was carried out in a cuvette of 1 cm path length. Photoluminescence measurements of crystals were performed by carefully preparing the sample with an optimized number of sub-millimeter-sized crystals and placing it at a designated orientation, wherein self-absorption could be attenuated. Gated emission measurements were carried out using a Horiba Jobin Yvon Fluorolog spectrometer equipped with a flash lamp with a pulse width of 3 μs. The crystal was sandwiched between two quartzs pieces for the measurements. Temperature-dependent gated measurements were carried out in the same instrument using a liquid nitrogen cryostat (Janis VNF-100). The gated measurements were carried out using 100 flash count, 2 mm slit width and 50 μs delay time.

1.1 X-ray Crystallography

High-quality crystals of P-Br_4 with appropriate dimensions were selected for the X-ray diffraction experiments. Crystallographic data collected are presented in the supporting information, Table S1. A single crystal was mounted using oil (Infineum V8512) on a glass fiber. All measurements were made on a CCD area detector with graphite monochromated Mo K_α radiation. The data was collected using Bruker APEXII detector and processed using APEX2 from Bruker. The structure was solved by direct method and expanded using the Fourier technique. The non-hydrogen atoms were refined anisotropically. Hydrogen atoms were included in idealized positions, but not refined. All programs used during the crystal structure analysis are incorporated into the WINGX software.[1] The full validation of CIF and structure factor of was performed using the check CIF utility and found to be free of major alert levels. 3D structure visualization and the exploration of the crystal packing of P-Br_4 were carried out using Mercury 2021.2.0.[2]

1.2 Computational Details

All the calculations are carried out in Gaussian 16 employing the CAM-B3LYP functional and def2svp basis set at the DFT level of theory unless stated otherwise. The natural transition orbitals (NTO) of P-Br_4 were obtained from the generated cube files of energy calculations. To compute long-range Coulombic coupling, an electronic energy transfer (EET) module available in the Gaussian 16 program is utilized.[3] TDDFT calculation is performed on monomers for the S_0 to S_1 transition where Coulombic coupling between the states is procured. UV spectrum generation and hole-electron analysis are carried out using Multiwfn version 3.7.[4] Electron and hole transfer coupling values were calculated by employing the CATNIP Tool version 1.9.[5] Both Multiwfn and CATNIP use post-processed Gaussian 16 output files for the respective analyses.

1.3 Noncovalent interaction (NCI) Plot[6]

NCI analysis employs an index based on electron density and its derivatives to identify noncovalent interactions. A two-dimensional plot of reduced electron density (s) against electron density (ρ) and the critical points are associated with the troughs appearing in the plot. Reduced electron density is given by:

$$s = \frac{1}{2(3\pi^2)^{1/3}} \frac{|\nabla\rho|}{\rho^{4/3}} \qquad \text{(Equation S1)}$$

Noncovalent interactions occur in the real space points where these troughs appear. The sign of the second derivative of ρ ($\nabla 2\rho$) is analyzed to distinguish attractive and repulsive interactions. The non-covalent interaction regions are represented in the plot as discs with colors ranging from blue (attractive) to red (repulsive), as in the VIBGYOR spectrum.

1.4 Hirshfeld Analysis[7, 8]

Important intermolecular interactions within the crystal structure of P-Br_4 were identified through Hirshfeld surface analysis using Crystal Explorer 3.1. The Hirshfeld surface is defined as a set of points in 3D space where the ratio of pro molecule and pro crystal electron densities is equal to 0.5. The exploration of intermolecular contacts is provided by mapping normalized contact distances (d_{norm}), which is a function of the closest distance from the point to the nuclei interior (d_i) and exterior (d_e) to the surface as well as on the van der Waals radii (r^{vdw}). 2D fingerprints were generated by deriving from the Hirshfeld surface by plotting the fraction of points on the surface as the function of d_i and d_e which provide a visual summary of intermolecular contacts within the crystal.

1.5 Energy Framework Analysis

The intermolecular interaction energies of P-Br_4 were estimated using the CE-B3LYP method using the 6-31G(d,p) basis set in the Crystal Explorer package.[9, 10] The components of interaction energies are scaled using the optimized scale factors for the CE-B3LYP method given by $E_{electrostatic}$ = 1.057, $K_{polarization}$ = 0.740, $K_{dispersion}$ = 0.871, and $K_{repulsion}$ = 0.618. Further, the intermolecular interaction topologies were visualized using the energy frameworks tool in CrystalExplorer. The intermolecular interaction energies of molecular pairs and interaction topologies represent molecular clusters around a central molecule in the crystal structures that make direct interactions.

1.6 Quantum Theory of Atoms in Molecules (QTAIM)[11]

The wave function generation for the molecules was carried out at CAM-B3LYP/def2svp using Gaussian 16[12] and the subsequent location of the critical points and the topology analysis were carried out using Multiwfn 3.7.[4] Quantum theory of atoms in molecules (QTAIM) analysis helps to understand the description of interatomic interaction in the single crystal X-ray structure. A bond is defined along the bond line between two nuclei, called a bond path, along which electron density is concentrated. The (3, -1) bond critical point (BCP) is a point along the bond path at the interatomic surface, where the shared electron density reaches a minimum. (3, +1) ring critical point (RCP) and (3, +3) cage critical point (CCP) represent critical points in the ring and cage respectively where the electron density is minimum. The physical characteristics of the critical points [the electron density at BCP, RCP, and CCP, ρ(r), and its Laplacian, $\nabla^2\rho(r)$ reveal the approximate measure of the amount of electron density built up in the bonding region and as such could be taken as characteristic of the bond. When $\nabla^2\rho(r) < 0$ and is large in magnitude, ρ(r) is also large which means that there is a concentration of electronic charge in the internuclear region. This is also an indication of a sharing of electronic charge between both nuclei that defines the covalent (polar) bond. When $\nabla^2\rho(r) > 0$ there is a depletion of electronic charge in the internuclear region and it indicates a closed shell interaction. The topological analysis of the electron density distribution has been viewed using VMD software.[13]

1.7 Symmetry Adapted Perturbation Theory (SAPT)[14]

SAPT(0) analysis was employed to determine the non-covalent interaction energies of dimer molecules. The SAPT module of the psi4[14] code was employed, with aug-cc-pVDZ basis set. SAPT(0) calculations provide the contributing components of interaction energy. The results obtained from SAPT(0) analysis are a second-order perturbation expansion constituting first-order electrostatic and exchange energy parts and second-order dispersion, induction, and their exchange counterparts as the perturbation terms.

$$E_{int}^{SAPT(0)} = E_{elec}^{(1)} + E_{ex}^{(1)} + E_{ind}^{(2)} + E_{ind-ex}^{(2)} + E_{dis}^{(2)} + E_{dis-ex}^{(2)} \qquad \text{(Equation S2)}$$

1.8 Excitonic Coupling Parameters[15, 16]

The excitonic coupling between the donor and acceptor was theoretically examined by evaluating the contributions from both long-range and short-range effects. To compute long-range Coulombic coupling, electronic energy transfer (EET) module available in Gaussian 16 program is utilized at CAM-B3LYP/def2svp. Electronic energy transfer (EET) or resonance energy transfer (RET) refers to the energy

transfer process from a photoexcited donor molecule to a nearby ground-state acceptor molecule. In Gaussian 16, the EET analysis employs a quantum mechanical model based on a DFT wavefunction description, incorporating a time-dependent variational approach. This involves performing an excited-state calculation on each fragment and subsequently computing all the couplings among the resulting states. $JCoul$ is the Coulombic coupling between electronic transitions where

$$J_{Coul} = \iint dr_1 dr_2 \frac{\rho_D^{tr}(r_1)\rho_A^{tr*}(r_2)}{|r_1 - r_2|} \qquad \text{(Equation S3)}$$

Where $\rho_D{}^{tr}(r_1)$ and $\rho_A{}^{tr}(r_2)$ are the transition densities (the diagonal element of the density matrix) respectively of donor and acceptor. TD-DFT calculation was performed on each of the dimers after defining each monomer as a fragment for the S0 to S1 transition and Coulombic coupling between the states with highest oscillator strength was procured.

The short-range exciton coupling stemming from the degree of overlap of wave functions on proximal molecules has a crucial role in defining the excitonic interaction and is determined as,

$$J_{CT} = \frac{-2t_e t_h}{E_{CT} - E_{S_1}} \qquad \text{(Equation S4)}$$

where t_e and t_h are the electron and hole-transfer coupling which depend on the LUMO-LUMO and HOMO-HOMO orbital overlap of the monomers, respectively, E_{CT}= 4.847 is the energy of the charge-transfer state (from the TheoDORE analysis), and E_{S_1}=3.7592 is the energy of the first Frenkel exciton state calculated from TD-DFT. The total coupling between neighboring molecules can be represented as,

$$J_{Total} = J_{Coul} + J_{CT} \qquad \text{(Equation S5)}$$

1.9 Anisotropic Charge Transport Mobility[17]

The charge transfer rate (k_i), which represents the rate of hole/electron hopping from a monomer to the ith neighbor was obtained through the Marcus-Hush equation:

$$k_i = \frac{t^2}{\hbar}\left(\frac{\pi}{\lambda k_B T}\right)^{\frac{1}{2}} e^{\frac{-\lambda}{4k_B T}} \qquad \text{(Equation S6)}$$

where t is the charge transfer coupling between the monomers of a dimer, λ is the reorganization energy for the hole (λ_h) or electron (λ_e) transport, k_B is the Boltzmann constant and T is the temperature (300 K). The reorganization energy can be calculated using the following formula:

$$\lambda_{\pm} = (E_0^* - E_0) + \left(E_{\pm}^* - E_{\pm}\right) \qquad \text{(Equation S7)}$$

in which E_0 and $E_{\pm}$ are the lowest energies of neutral and cationic/anionic species, respectively. For hole reorganization energy (λ_h), E_0^* is the energy of a neutral molecule with cation geometry, while for the electron reorganization energy (λ_e), E_0^* corresponds to the energy of the neutral molecule with anion geometry. The reorganization energy for P-Br$_4$ (λ_h = 0.216 eV, λ_e = 0.164 eV) was calculated.

The anisotropic mobility is calculated using the following formula:

$$\mu_{\phi} = \frac{e}{2k_BT}\sum_i k_i\, r_i^2 P_i cos^2\gamma_i cos^2(\theta_i - \phi) \quad \text{(Equation S8)}$$

Where γ_i is the angle between the charge hopping pathway and plane of interest, ϕ is the orientation angle of the transport channel relative to the reference axis and θ_i are the angles between the projected hopping paths of different dimers and the reference axis. P_i is the charge hopping probability:

$$P_i = \frac{k_i}{\sum_i k_i} \quad \text{(Equation S9)}$$

2.0 TheoDORE Analysis[16, 18]

The excited state dynamics of the monomers of P-Br_4 is analyzed using TheDORE. The dihydropentacene core was considered as one fragment, and four bromines were the other fragment. The parameters used to investigate the excited state characteristics are participation ratio (P_R), mean position (POS) of initial orbital (hole) and final orbital (electron), and charge transfer character (CT). The magnitude of P_R relates to the number of fragments participating in the excitation, hence, in our investigation, the P_R ranges from 1 to 2. POS provides the mean position of the hole and electron for a particular excitation. Charge transfer states and delocalized Frenkel states show POS = 1.5. If the Frenkel state is localized on monomer A, then POS = 1, and if localized on monomer B, POS = 2, for a dimer AB. Finally, CT is related to the total weight of configurations where initial and final orbitals are situated on different fragments. A CT value of 1 denotes the presence of a charge-separated state, and CT = 0 refers to Frenkel states. Further, electron-hole correlation plots were generated to analyze the excitonic character for P-Br_4. If the shade is present only in the diagonal parts, the excitonic character is Frenkel. Off-diagonal shades refer to a CT state.

2.1 Electrostatic Potential Map

The electrostatic potential (ESP) map illustrates the charge distribution of molecules in three dimensions. These maps allow us to visualize variably charged regions of a molecule. Knowledge of the charge distributions can be used to determine how molecules interact with one another. Gaussian[12] supports the cube keyword to generate the cubes separately from the formatted checkpoint file (generated from energy calculation with cam-b3lyp/def2svp level of theory using the cubegen utility program. This allows for the generation of electrostatic surface potential mapping of the molecule.

Section B: Synthesis and Characterization

Scheme S1: Shows the synthesis of Pentacenedione and P-Br_4.

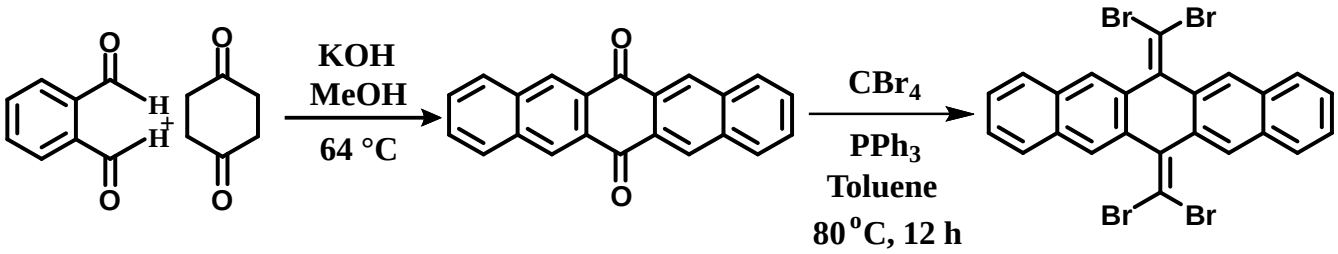

Synthesis of Pentacene-6,13-dione

4.02g (30 mmol) of ortho-phthalaldehyde and 1.68 g (15.00 mmol) of cyclohexanedione were dissolved in 450 ml of methanol. 15 ml of a 15% aqueous KOH solution was added, upon which the solution turned brownish and a yellow/orange precipitate formed. For completion of the reaction, the mixture was stirred for an additional 4 h at 64 °C. After cooling the solid was filtered and thoroughly washed with acetone, giving the product as a yellow solid (3.95 g, 12.80 mmol; 85%)

^{1}H NMR (500 MHz, $CDCl_3$, ppm) δ = 8.96 (s, 4H), 8.15-8.13 (m, 4H), 7.73-7.71(m, 4H).

HRMS (APCI) *m/z* calculated for $C_{22}H_{12}O_2$ [$(M+H)^+$] = 309.0916, found: 309.0903

Synthesis of 6,13-bis (dibromomethylene)-6, 13-dihydropentacene

CBr_4 (4.30 g, 12.90 mmol), PPh_3 (6.80 g, 25.80 mmol), and anhydrous toluene (150 ml) were added to a 250 ml two-necked round-bottom flask and stirred at room temperature for 5 minutes. 6, 13-pentacenequinone was then added to the flask and the solution was stirred at 80 °C for 12 hours. The solution was cooled to room temperature, with the precipitate removed by filtration and rinsed with toluene. The filtrate was dried under reduced pressure, and the crude product was subjected to column chromatography (CH_2Cl_2: Hexane=1: 5).

^{1}H NMR (500 MHz, $CDCl_3$, ppm) δ = 8.28 (s, 4H), 7.86-7.84 (m, 4H), 7.52-7.50 (m, 4H).

HRMS (APCI) *m/z* calculated for $C_{24}H_{12}Br_4$ [M^+] = 619.7673, found: 619.7630

Section C: Tables

Table S1: Crystallographic data and refinement parameters for P-Br_4.

Parameters	P-Br_4
Formula	C_{24} H_{12} Br_4
Formula wt.	619.98
Crystal system	Monoclinic
Space group, Z	P c, 4
a, Å	7.9052(3)
b, Å	12.3181(4)
c, Å	22.0431(6)
α, deg	90.00
β, deg	90.0060(10)
γ, deg	90.00
V, $Å^3$	2146.49
Temp, K	301(2)
d_{calcd}, mg/m^3	1.918
no. of reflections collected	43873
Max. and min. transmission	0.715 and 0.228
Absolute structure parameter	0.022(5)
Independent reflections	7343 [R(int) = 0.0532]
Final R indices [I>2sigma(I)]	R1 = 0.0340, wR2 = 0.0773
R indices (all data)	R1 = 0.0413, wR2 = 0.0809
goodness of fit	1.101
CCDC deposition number	2414288

Table S2: Interaction energies in selected dimers determined by SAPT (0)/aug-cc-pVDZ calculations and SAPT(0) energy components for crystalline P-Br_4.

Dimers	Electrostatic (kJ/mol)	Exchange (kJ/mol)	Induction (kJ/mol)	Dispersion (kJ/mol)	$E_{int}^{SAPT(0)}$ (kJ/mol)
1	-22.690	56.010	-5.629	-93.409	-65.718
2	-12.266	26.416	-3.584	-45.594	-35.030
3	-4.455	9.272	-1.166	-13.432	-9.781

Table S3: Relative % intermolecular interactions obtained from Hirshfeld analysis.

%C•••Br	%C•••H	%H•••H	%Br•••Br	%H•••Br
13.6	30	16.3	4	35.2

Table S4: Intermolecular interaction energies of molecular pairs in P-Br_4 calculated using energy framework analysis.

	N	Symop	R	Electron Density	E_ele	E_pol	E_dis	E_rep	E_tot
	1	-	8.04	B3LYP/6-31G(d,p)	-9.9	-1.3	-46.0	31.9	-31.8
	1	-	6.68	B3LYP/6-31G(d,p)	-15.8	-1.5	-67.2	55.5	-42.0
	2	x, y, z	7.91	B3LYP/6-31G(d,p)	-6.1	-0.7	-31.0	19.6	-21.9
	1	-	14.01	B3LYP/6-31G(d,p)	-0.6	-0.1	-3.3	0.0	-3.6
	2	x, y, z	12.32	B3LYP/6-31G(d,p)	0.5	-0.2	-10.4	0.0	-8.7
	1	-	6.68	B3LYP/6-31G(d,p)	-16.0	-1.5	-67.6	56.0	-42.3
	1	-	8.04	B3LYP/6-31G(d,p)	-10.0	-1.3	-46.1	32.4	-31.7
	1	-	10.69	B3LYP/6-31G(d,p)	-8.2	-1.0	-33.5	22.1	-25.0
	2	x, -y, z+1/2	11.78	B3LYP/6-31G(d,p)	-0.2	-0.1	-4.3	0.2	-3.9
	1	-	10.68	B3LYP/6-31G(d,p)	-8.2	-1.0	-33.6	22.2	-25.0
	1	-	14.01	B3LYP/6-31G(d,p)	0.1	-0.1	-3.3	0.0	-2.9
	2	x, -y, z+1/2	13.72	B3LYP/6-31G(d,p)	2.7	-0.2	-3.7	0.0	-0.5

Scale factors for benchmarked energy models
See Mackenzie et al. IUCrJ (2017)

Energy Model	k_ele	k_pol	k_disp	k_rep
CE-HF ... HF/3-21G electron densities	1.019	0.651	0.901	0.811
CE-B3LYP ... B3LYP/6-31G(d,p) electron densities	1.057	0.740	0.871	0.618

Table S5: Calculated topological properties of electron density function for the intermolecular interactions forming bifurcating synthons in P-Br_4.

Synthon		Interactions	d(Å)	ρ(r) ($eÅ^{-3}$)	∇^2 ρ(r) ($eÅ^{-5}$)
Dimer1	Bond Critical Points (BCPs)	CP-97 Br38●●●Br77	4.306	+0.0028745	+0.0081616
		CP-143 Br78●●●Br40	3.766	+0.0057782	+0.0166259
		CP-163 Br78●●●Br39	3.640	+0.0079865	+0.0213023
	Ring Critical Points (RCPs)	CP-146 Br39-Br40-Br78	-	+0.0056102	+0.0178786

Table S6: Computed long-range Coulombic ($J_{Coulomb}$) and short-range charge transfer integral (t_e and t_h) for the dimers of P-Br_4.

P-Br_4	t_e (cm^{-1})	t_h (cm^{-1})	Coulombic Coupling Energy (cm^{-1})
Dimer1	120.9	177.4	602.10
Dimer2	-72.737	-296.581	262.938
Dimer3	-24.438	-13.434	-116.935

Table S7: Mean position (POS), participation ratio (P_R), charge transfer character (CT), and exciton character of excited states in P-Br_4 monomer and dimer.

	Monomer			Dimer			
State	POS	PR	CT	E (eV)	POS	PR	CT
S_1	1.947	1.113	0.100	4.257	1.002	1.004	0.004
S_2	1.934	1.143	0.122	4.266	1.015	1.030	0.005
S_3	1.960	1.082	0.074	4.293	1.997	1.006	0.004
S_4	1.954	1.096	0.085	4.313	1.985	1.031	0.006
S_5	1.849	1.353	0.269	4.327	1.997	1.006	0.003
S_6	1.811	1.445	0.300	4.347	1.005	1.011	0.007
S_7	1.908	1.908	0.163	4.375	1.073	1.156	0.006
S_8	1.564	1.915	0.478	4.393	1.928	1.155	0.006
S_9	1.901	1.222	0.170	4.609	1.319	1.763	0.012
S_{10}	1.718	1.679	0.326	4.708	1.683	1.763	0.030
S_{11}	1.928	1.154	0.129	4.847	1.501	1.053	0.949

Table S8: Vertical excitation energy of CAM-B3LYP/def2svp-optimized geometry of P-Br_4.

Singlet	Energy (eV)	Triplet	TDA
S_1	3.759	T_1	2.295
S_2	3.774	T_2	2.594
S_3	3.888	T_3	2.808
S_4	3.990	T_4	3.120
S_5	4.026	T_5	3.466
S_6	4.203	T_6	3.734
S_7	4.230	T_7	4.198
S_8	4.738	T_8	4.260
S_9	4.809	T_9	4.278
S_{10}	4.886	T_{10}	4.365

Table S9: Spin-orbit coupling values between the singlet and triplet states of P-Br_4.

Transition	cm^{-1}	Transition	cm^{-1}
$\langle S_1 \vert H_{soc} \vert T_1 \rangle$	0.188	$\langle S_2 \vert H_{soc} \vert T_1 \rangle$	34.685
$\langle S_1 \vert H_{soc} \vert T_2 \rangle$	20.605	$\langle S_2 \vert H_{soc} \vert T_2 \rangle$	0.119
$\langle S_1 \vert H_{soc} \vert T_3 \rangle$	11.632	$\langle S_2 \vert H_{soc} \vert T_3 \rangle$	1.238
$\langle S_1 \vert H_{soc} \vert T_4 \rangle$	0.050	$\langle S_2 \vert H_{soc} \vert T_4 \rangle$	9.151
$\langle S_1 \vert H_{soc} \vert T_5 \rangle$	8.179	$\langle S_2 \vert H_{soc} \vert T_5 \rangle$	31.852
$\langle S_1 \vert H_{soc} \vert T_6 \rangle$	35.940	$\langle S_2 \vert H_{soc} \vert T_6 \rangle$	0.166
$\langle S_1 \vert H_{soc} \vert T_7 \rangle$	0.140	$\langle S_2 \vert H_{soc} \vert T_7 \rangle$	15.010
$\langle S_1 \vert H_{soc} \vert T_8 \rangle$	2.600	$\langle S_2 \vert H_{soc} \vert T_8 \rangle$	9.971
$\langle S_1 \vert H_{soc} \vert T_9 \rangle$	78.576	$\langle S_2 \vert H_{soc} \vert T_9 \rangle$	0.800
$\langle S_1 \vert H_{soc} \vert T_{10} \rangle$	46.583	$\langle S_2 \vert H_{soc} \vert T_{10} \rangle$	0.261

Section D: Figures

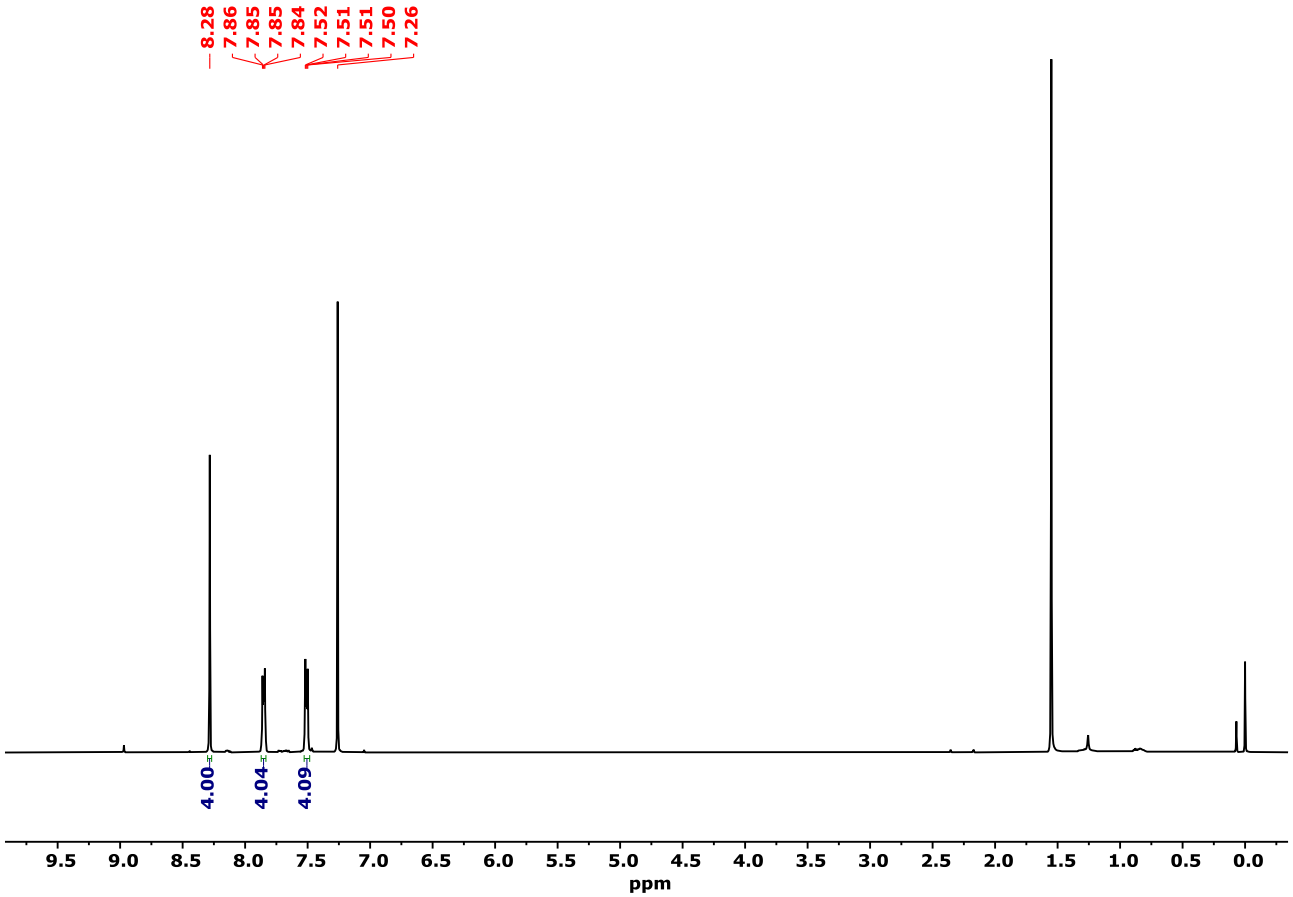

Fig. S1: ^{1}H NMR spectrum of P-Br_4 in $CDCl_3$.

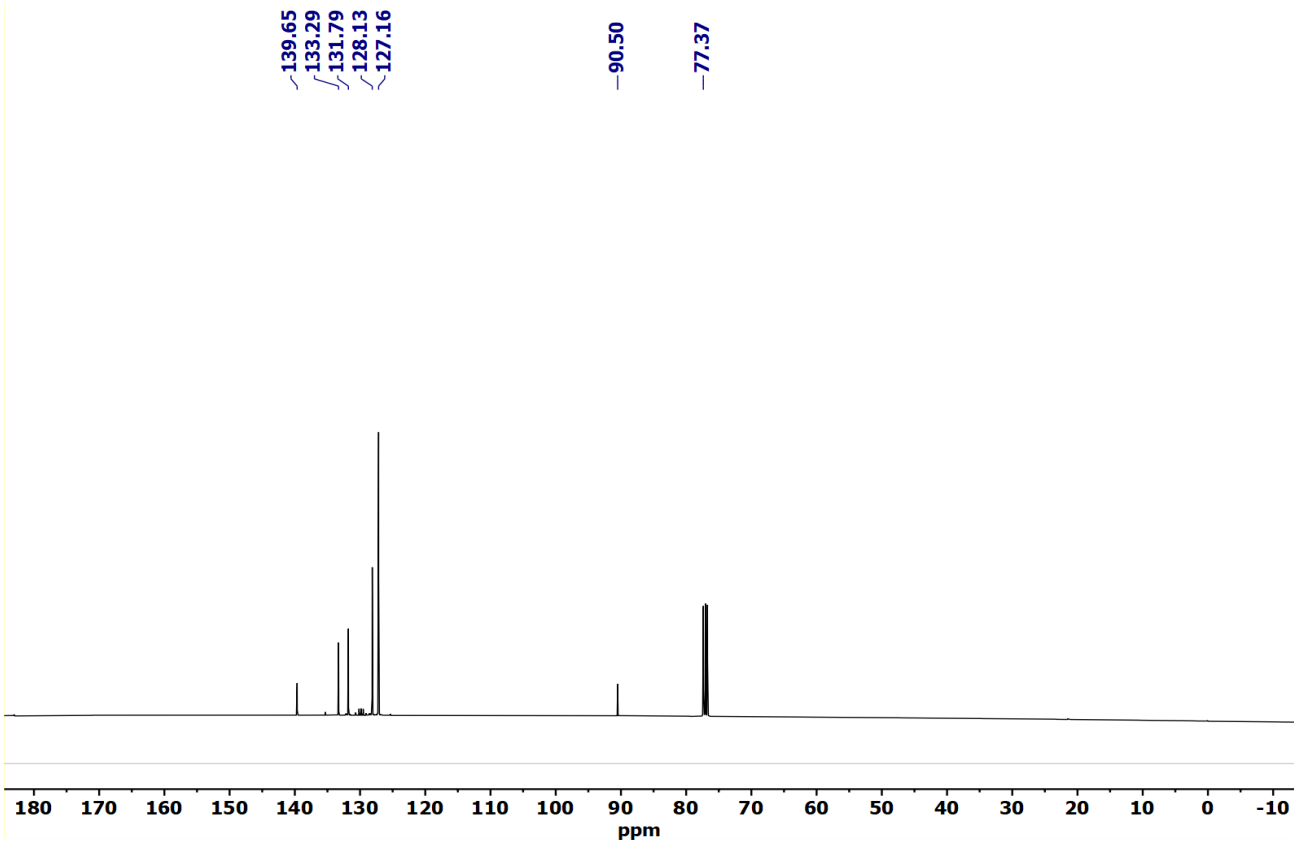

Fig. S2: ^{13}C NMR spectrum of P-Br_4 in $CDCl_3$.

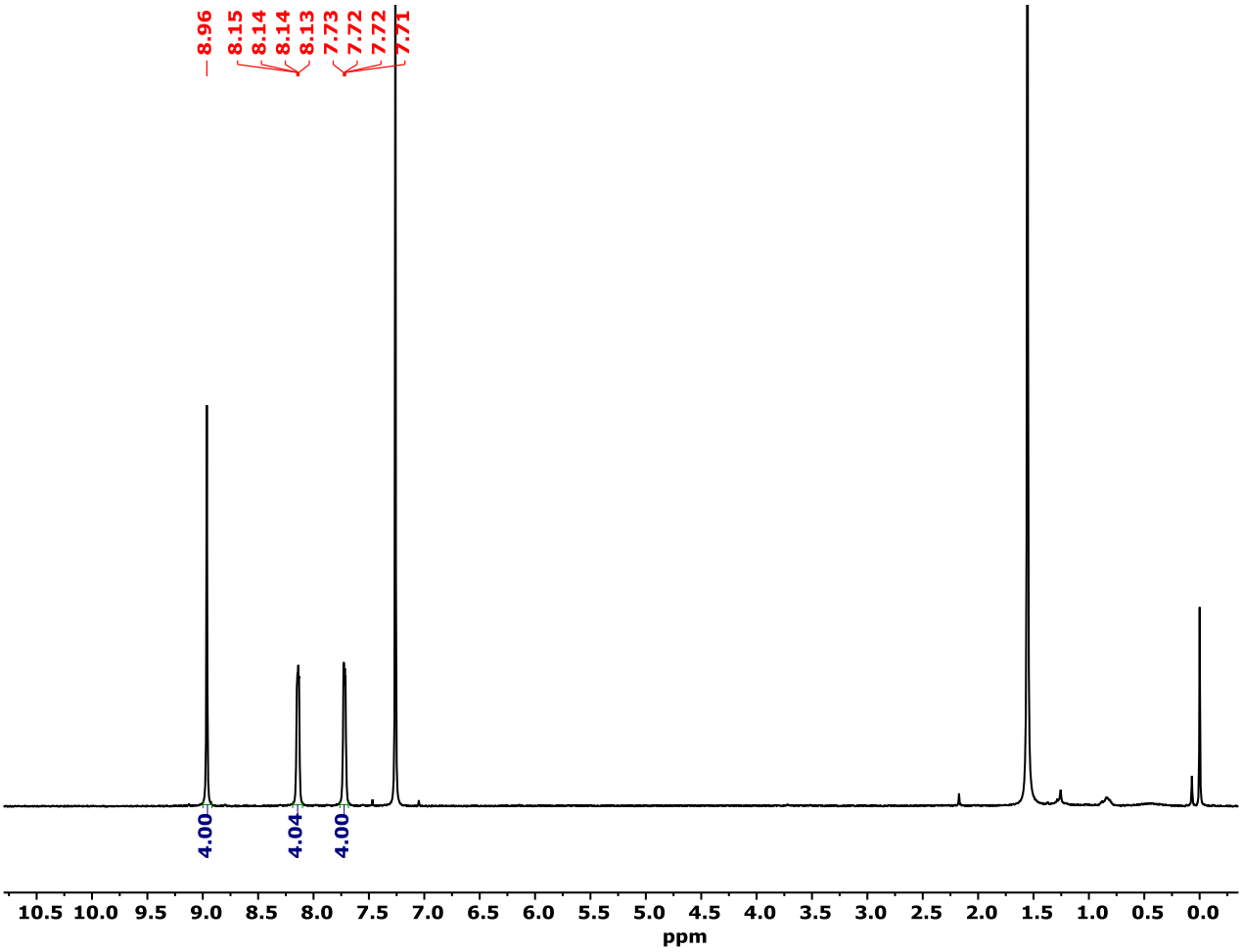

Fig. S3: ^{1}H NMR spectrum of Pentacene-6,13-dione in $CDCl_3$.

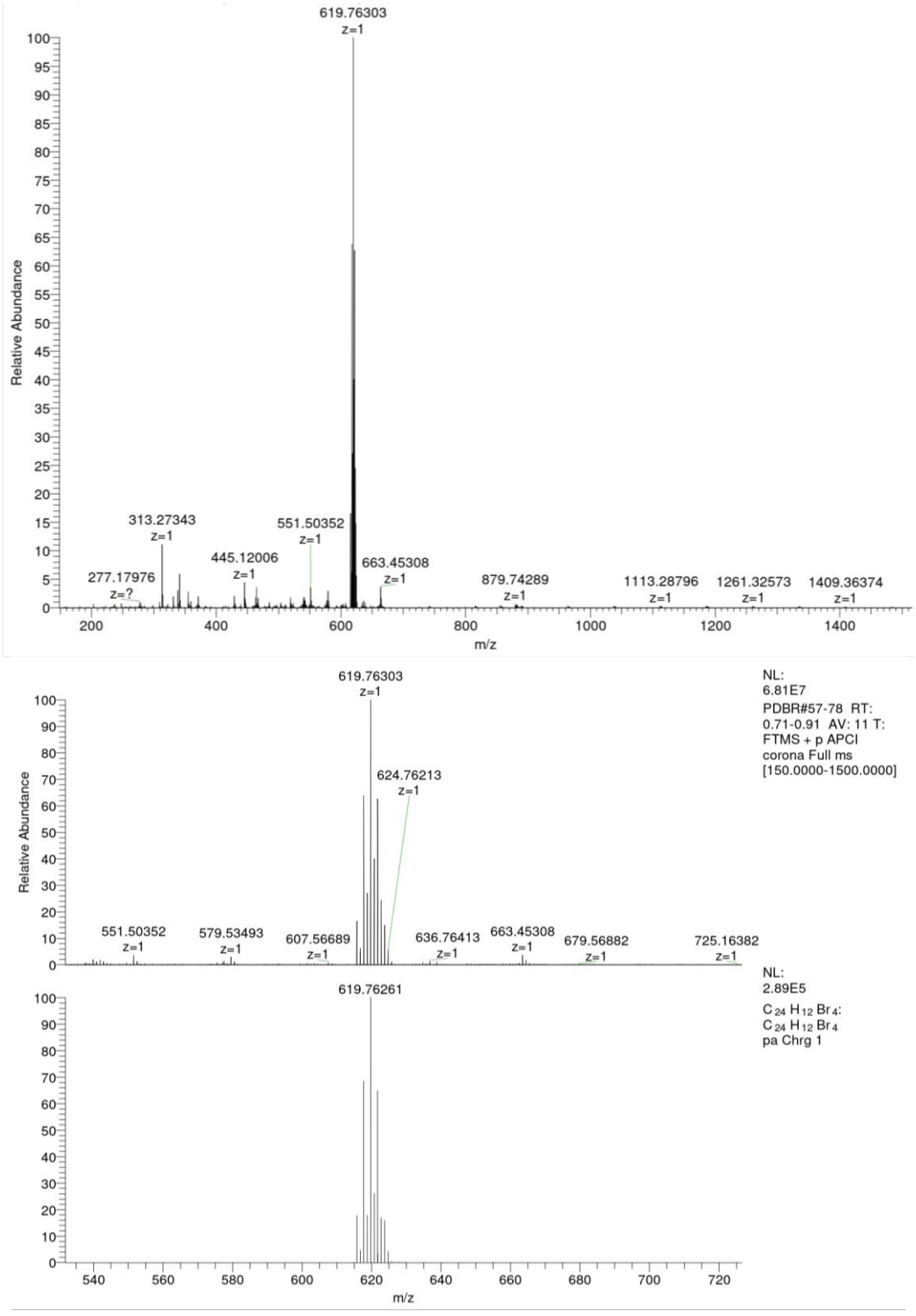

Fig. S4: HRMS spectrum of P-Br_4.

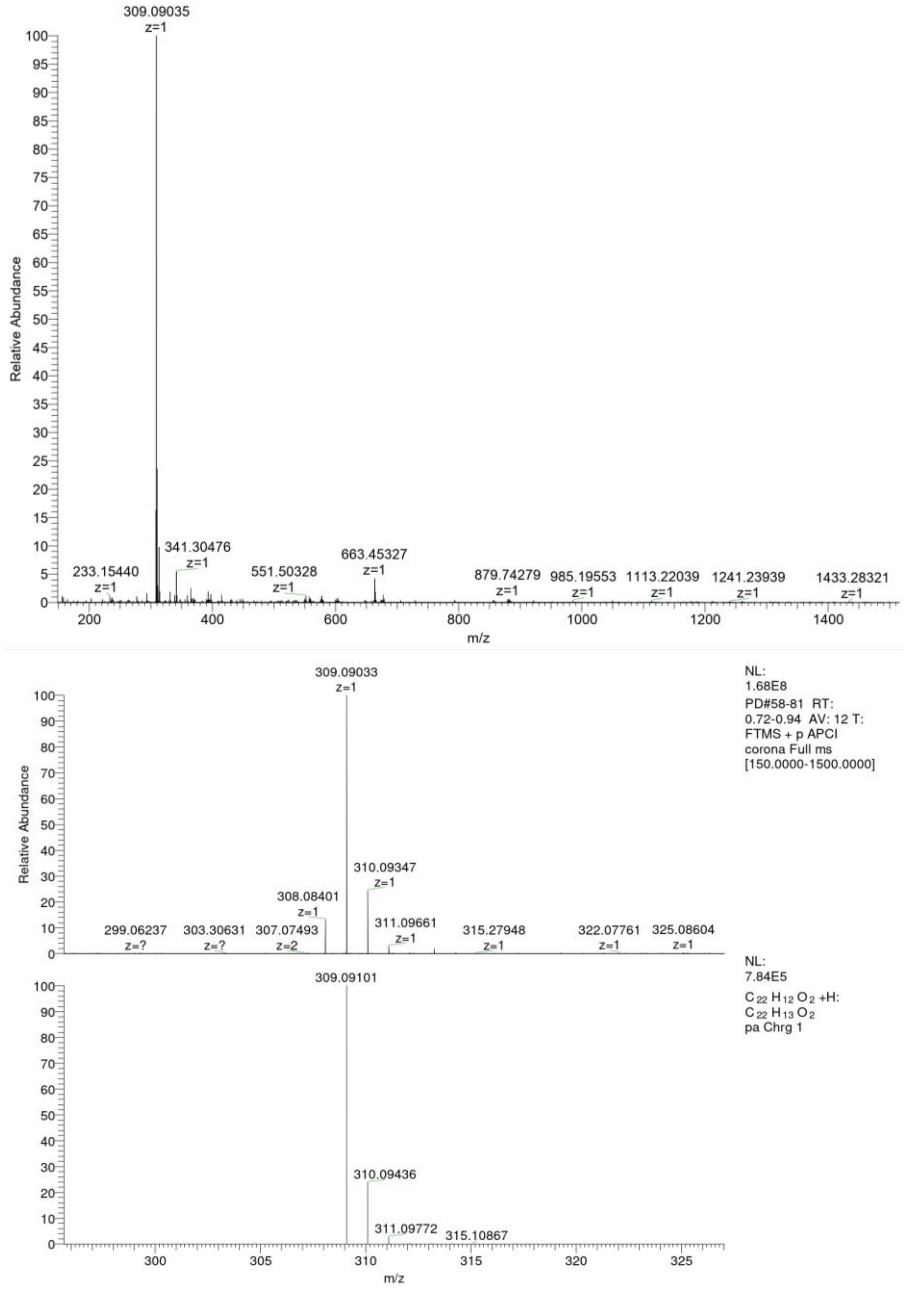

Fig. S5: HRMS spectrum of Pentacene-6,13-dione

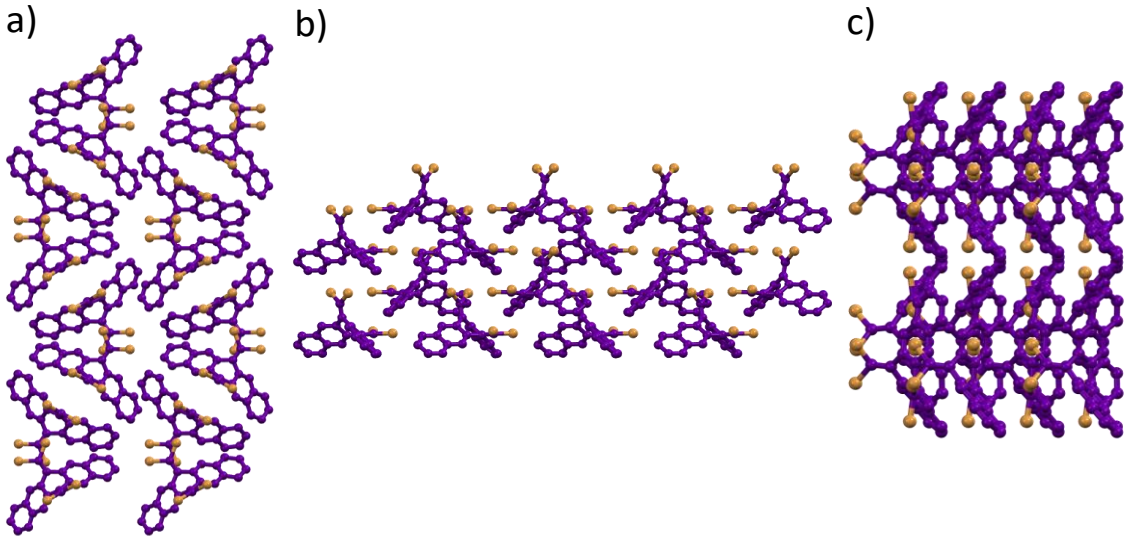

Fig. S6: Crystal packing of P-Br_4 viewed along a) a, b) b and c) c axis respectively.

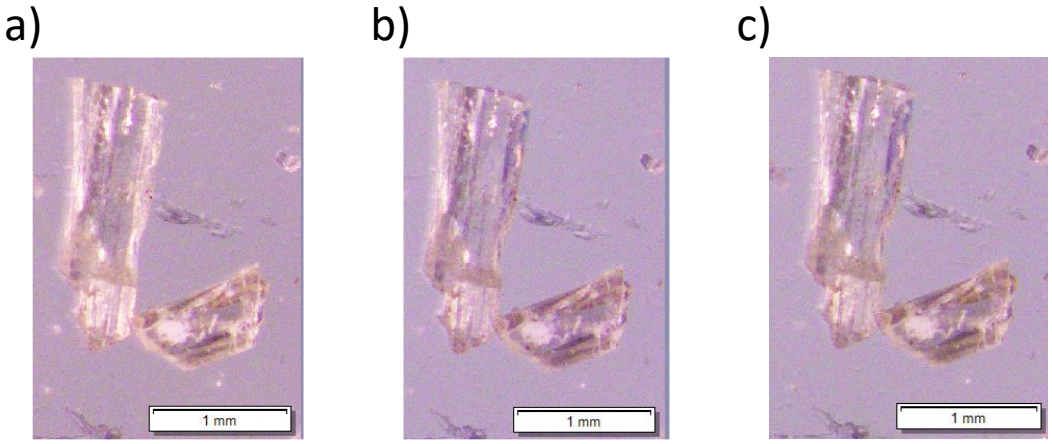

Fig. S7 a) Image of the PBr_4 crystal under daylight, b) UV excitation, and c) after removal of the UV light.

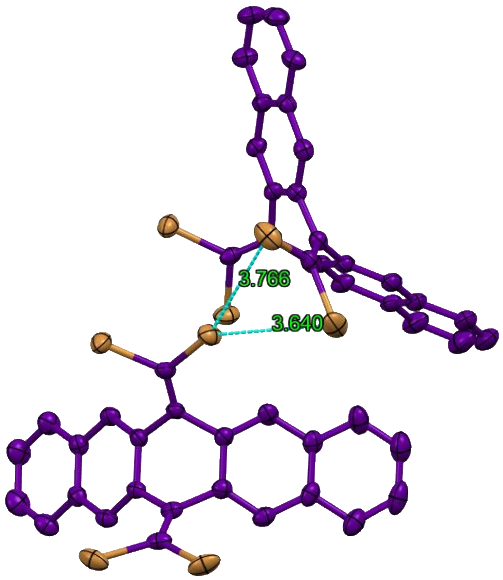

Fig. S8: A bifurcating synthon formed through Br···Br interactions with distance ($d_{Br\cdots Br}$) as 3.640 Å and 3.766 Å.

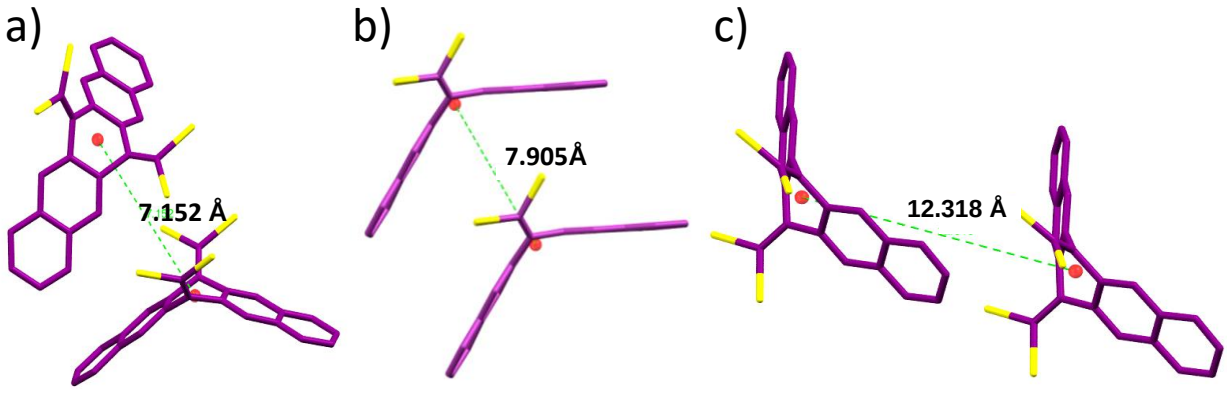

Fig. S9: a) Dimer-1 b) Dimer-2 and c) Dimer-3 with centroid to centroid distance.

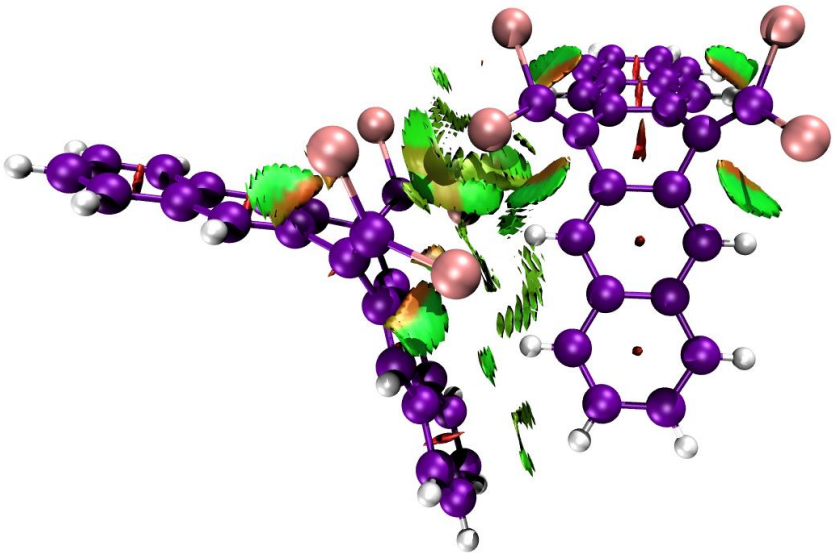

Fig. S10: NCI analysis of P-Br_4 dimer.

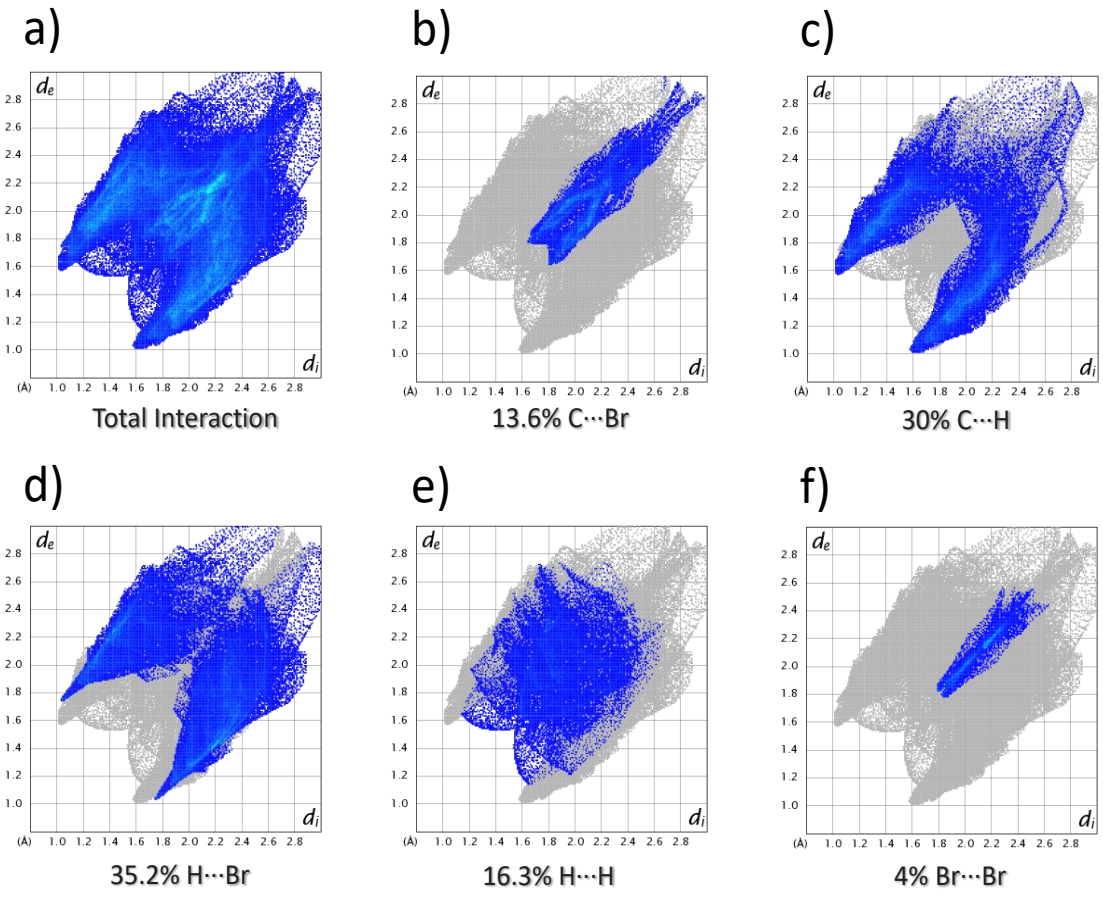

Fig. S11: Hirshfeld 2D fingerprint plots a) Total, b) C•••Br, c) C•••H, d) H•••Br e) H•••H and f) Br•••Br interactions of crystalline P-Br_4.

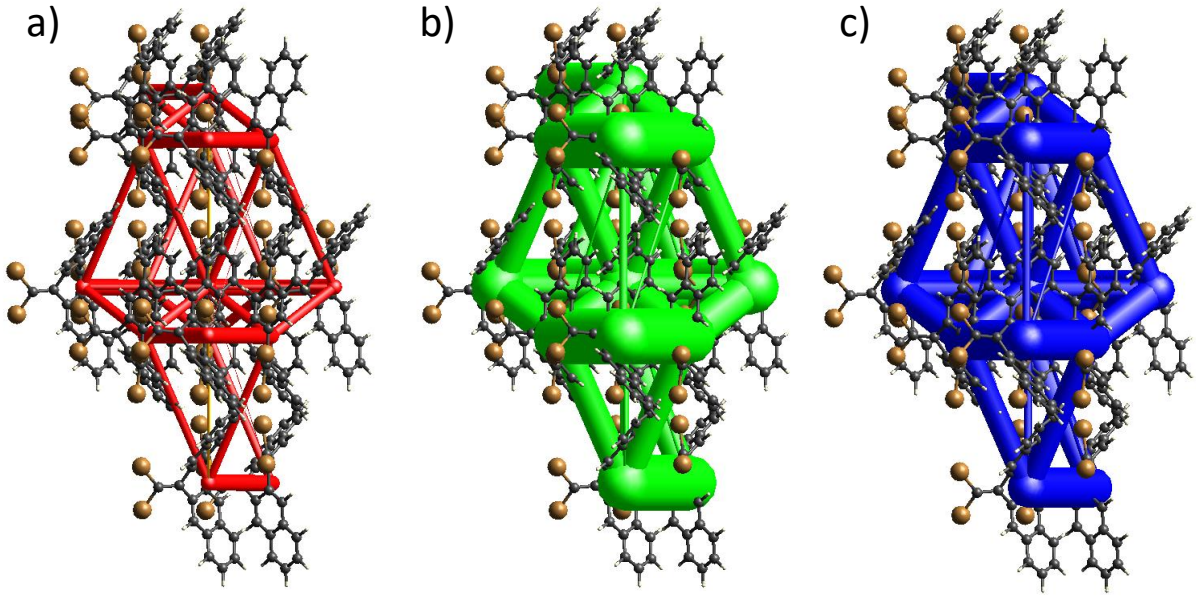

Fig. S12: Energy frameworks calculated for P-Br_4 crystal a) Coulombic component (red), b) dispersion component (green), and c) total energy (blue).

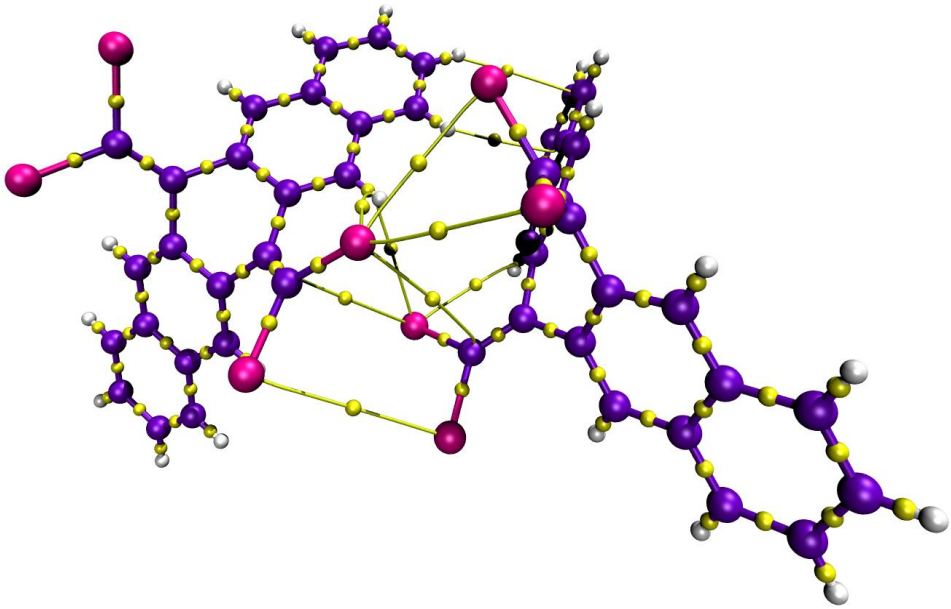

Fig. S13: QTAIM topological plot of P-Br_4 dimer where the small yellow circles indicate bond critical points and large circles correspond to atomic nuclei (C, H, and Br). The yellow lines represent bond paths.

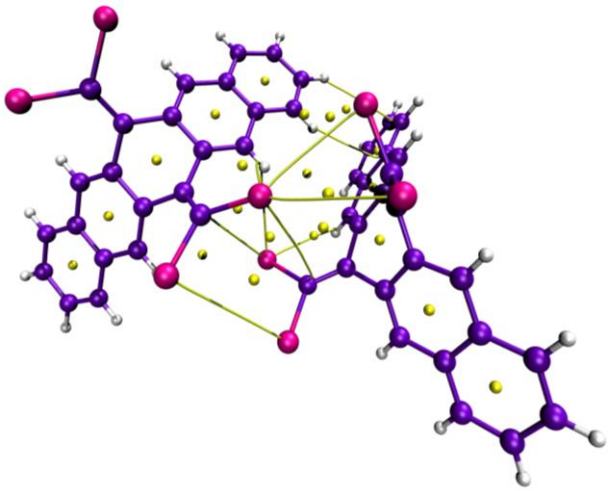

Fig. S14: QTAIM topological plot of P-Br_4 dimer where the small yellow circles indicate ring critical points and large circles correspond to atomic nuclei (C, H, and Br).

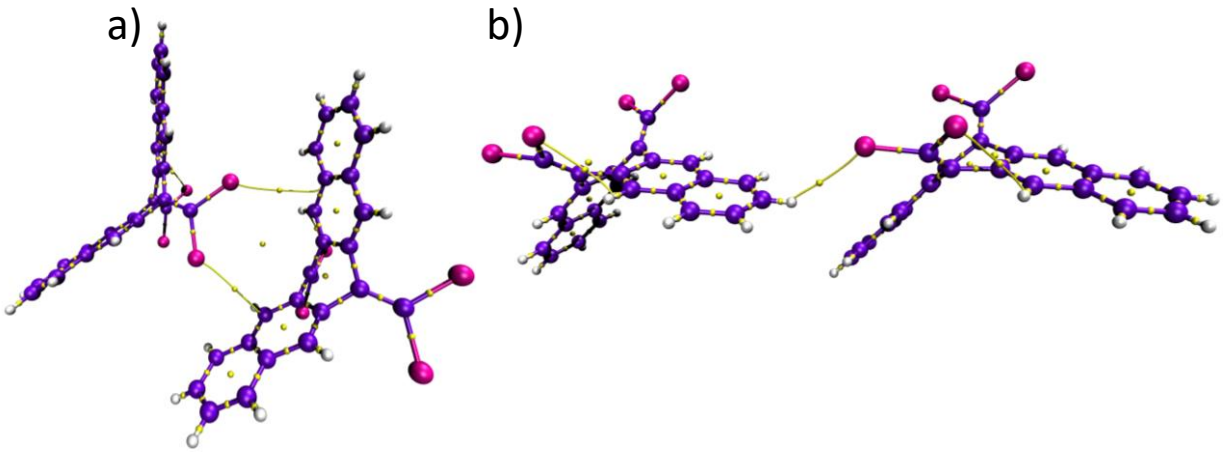

Fig. S15: QTAIM topological plots of P-Br_4 dimer2 and dimer3 where the small yellow circles indicate critical points and large circles correspond to atomic nuclei (C, H, and Br). The yellow lines represent bond paths.

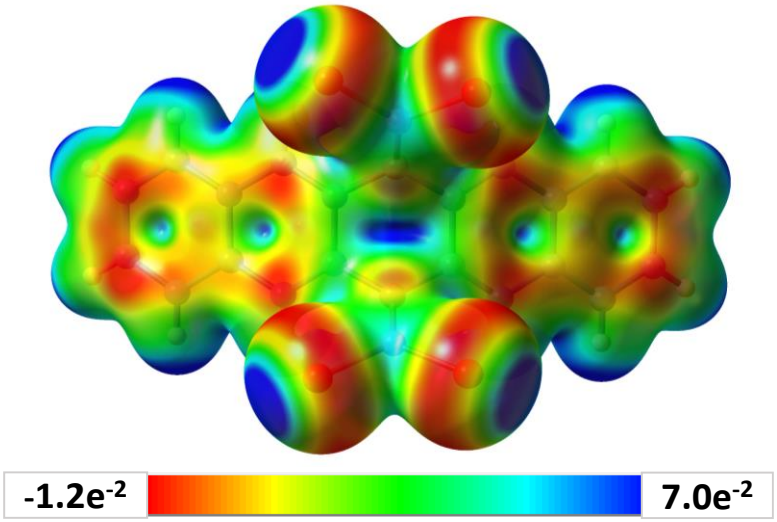

Fig. S16: Electrostatic surface potential (ESP) plot of P-Br_4.

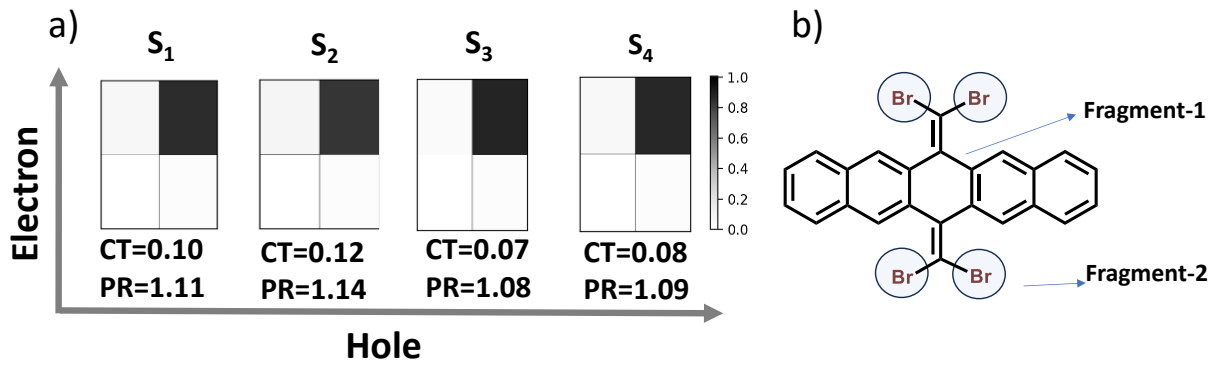

Fig. S17: a) Electron-hole correlation plots of excited states of P-Br_4. and b) Fragments used for analysis.

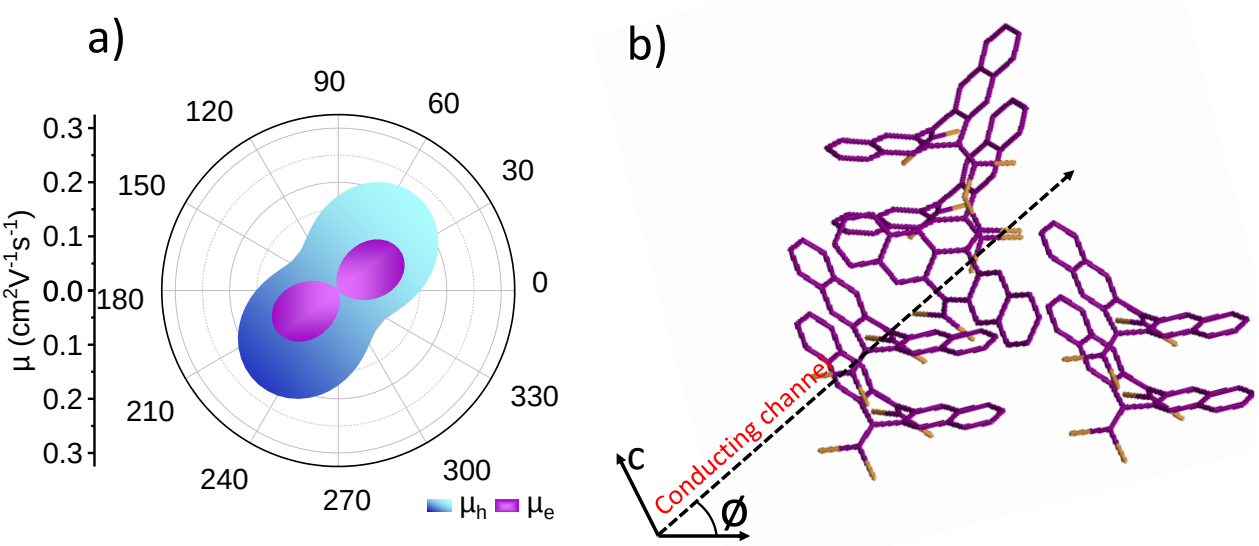

Fig. S18: (a) Anisotropic hole (μ_h, blue) and electron (μ_e, violet) mobility for P-Br_4 and (b) representation of conducting channel.

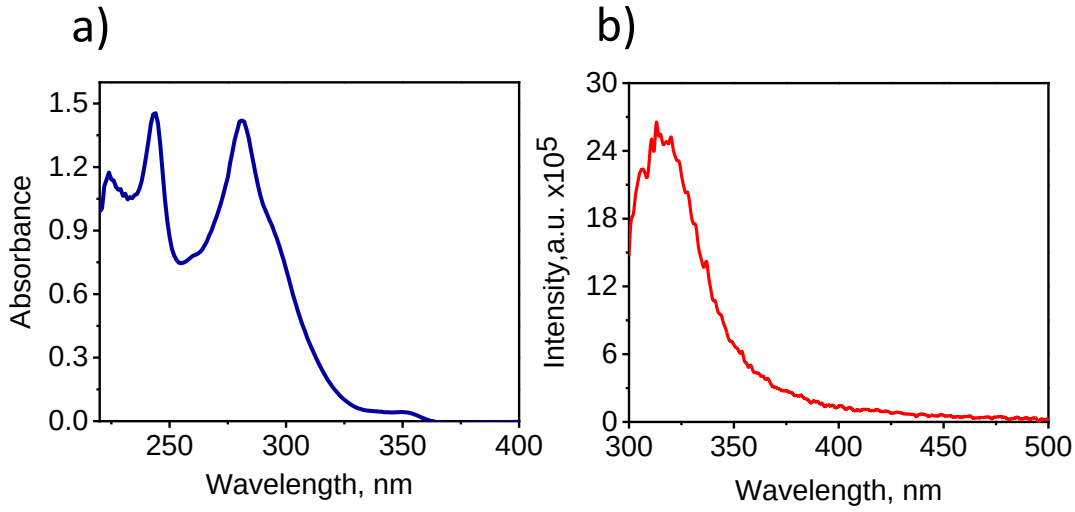

Fig. S19: a) UV-VIS absorption and b) emission spectra of P-Br_4 in THF solution.

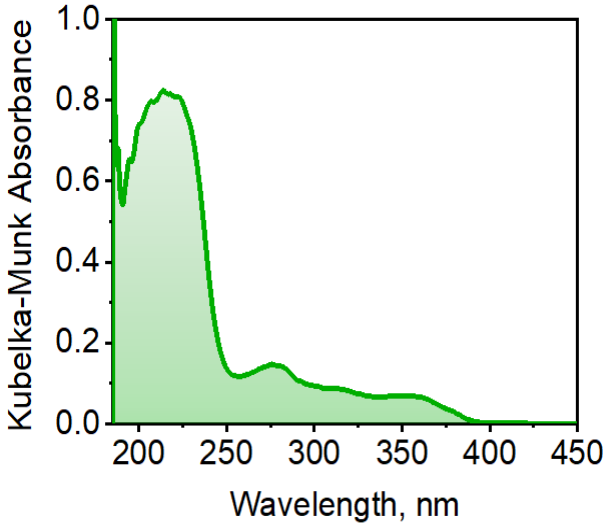

Fig. S20: Kubelka-Munk transformed diffuse reflectance spectrum of P-Br_4 crystal.

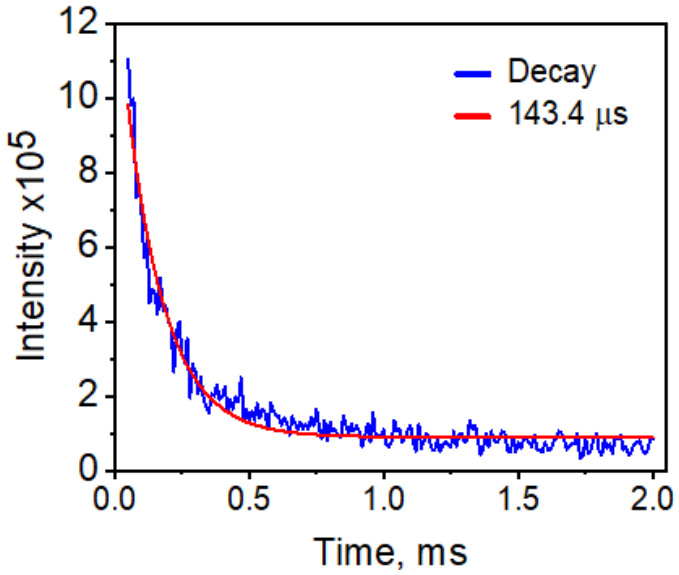

Fig. S21: Room-temperature phosphorescence decay of P-Br_4 crystal.

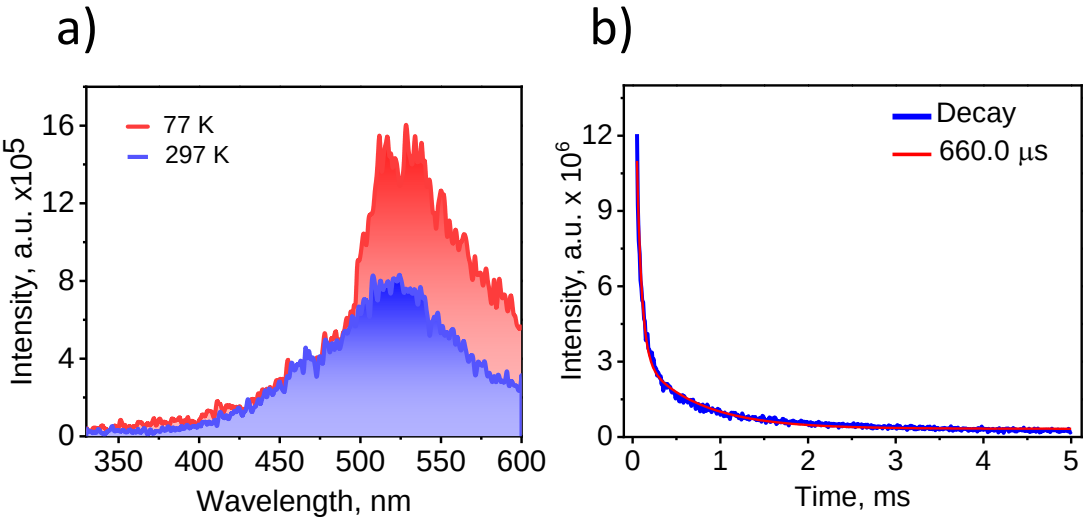

Fig. S22: a) Room-temperature and 77 K phosphorescence spectra and b) 77 K phosphorescence decay of P-Br_4 crystal.

Coordinates

0 1

C	-5.52599700	0.70728500	2.87337200
C	-5.52599700	-0.70728300	2.87337200
C	-4.47816700	-1.40143800	2.31855300
C	-3.38258300	-0.71447400	1.73495400
C	-3.38258300	0.71447500	1.73495300
C	-4.47816700	1.40144000	2.31855100
C	-2.28093000	-1.39913400	1.16497000
C	-1.22700800	-0.71677300	0.60365000
C	-1.22700800	0.71677400	0.60365000
C	-2.28093000	1.39913500	1.16496900
C	0.00000000	-1.37190800	0.07043700
C	1.22700800	-0.71677400	0.60365000
C	1.22700800	0.71677300	0.60365000
C	0.00000000	1.37190800	0.07043700
C	2.28093000	-1.39913500	1.16496900
C	3.38258300	-0.71447500	1.73495300
C	3.38258300	0.71447400	1.73495400
C	2.28093000	1.39913400	1.16497000
C	4.47816700	-1.40144000	2.31855100
C	5.52599700	-0.70728400	2.87337200
C	5.52599700	0.70728300	2.87337200
C	4.47816700	1.40143800	2.31855300
C	0.00000100	2.35187300	-0.84993300
C	-0.00000100	-2.35187300	-0.84993300
Br	1.58302800	3.09581000	-1.61883200
Br	-1.58302600	3.09581200	-1.61883200
Br	1.58302600	-3.09581200	-1.61883200
Br	-1.58302800	-3.09581000	-1.61883200
H	-6.35910200	1.24235000	3.31473300
H	-6.35910200	-1.24234700	3.31473400
H	-4.47610300	-2.48625700	2.31807700
H	-4.47610300	2.48625900	2.31807500
H	-2.27258600	-2.48150100	1.19181500
H	-2.27258600	2.48150200	1.19181400
H	2.27258600	-2.48150200	1.19181400
H	2.27258600	2.48150100	1.19181500
H	4.47610300	-2.48625900	2.31807500
H	6.35910200	-1.24234900	3.31473300
H	6.35910200	1.24234800	3.31473400
H	4.47610300	2.48625800	2.31807700

References

1. L. Farrugia, *Journal of Applied Crystallography*, 1999, **32**, 837-838.
2. I. J. Bruno, J. C. Cole, P. R. Edgington, M. Kessler, C. F. Macrae, P. McCabe, J. Pearson and R. Taylor, *Acta Crystallogr. B*, 2002, **58**, 389-397.
3. Gaussian 16, Revision C.01, M. J. Frisch, G. W. Trucks, H. B. Schlegel, G. E. Scuseria, M. A. Robb, J. R. Cheeseman, G. Scalmani, V. Barone, G. A. Petersson, H. Nakatsuji, X. Li, M. Caricato, A. V. Marenich, J. Bloino, B. G. Janesko, R. Gomperts, B. Mennucci, H. P. Hratchian, J. V. Ortiz, A. F. Izmaylov, J. L. Sonnenberg, D. Williams-Young, F. Ding, F. Lipparini, F. Egidi, J. Goings, B. Peng, A. Petrone, T. Henderson, D. Ranasinghe, V. G. Zakrzewski, J. Gao, N. Rega, G. Zheng, W. Liang, M. Hada, M. Ehara, K. Toyota, R. Fukuda, J. Hasegawa, M. Ishida, T. Nakajima, Y. Honda, O. Kitao, H. Nakai, T. Vreven, K. Throssell, J. A. Montgomery, Jr., J. E. Peralta, F. Ogliaro, M. J. Bearpark, J. J. Heyd, E. N. Brothers, K. N. Kudin, V. N. Staroverov, T. A. Keith, R. Kobayashi, J. Normand, K. Raghavachari, A. P. Rendell, J. C. Burant, S. S. Iyengar, J. Tomasi, M. Cossi, J. M. Millam, M. Klene, C. Adamo, R. Cammi, J. W. Ochterski, R. L. Martin, K. Morokuma, O. Farkas, J. B. Foresman, and D. J. Fox, Gaussian, Inc., Wallingford CT, 2016.
4. T. Lu and F. Chen, *Journal of Computational Chemistry*, 2012, **33**, 580-592.
5. GitHub - JoshuaSBrown/QC_Tools: This small repository provides functionality for calculating the charge transfer integrals between two molecules. https://github.com/JoshuaSBrown/QC_Tools (accessed Apr 15, 2020).
6. J. Contreras-García, E. R. Johnson, S. Keinan, R. Chaudret, J.-P. Piquemal, D. N. Beratan and W. Yang, J. *Chem. Theory Comput.,* 2011, 7**,** 625-632.
7. S. K. Rajagopal, A. M. Philip, K. Nagarajan and M. Hariharan, C*hem. Commun.,* 2014, 5**0,** 8644-8647.
8. M. A. Spackman and D. Jayatilaka, C*rystEngComm,* 2009, 1**1,** 19-32.
9. C. F. Mackenzie, P. R. Spackman, D. Jayatilaka and M. A. Spackman, I*UCrJ,* 2017, 4**,** 575-587.
10. M. J. Turner, S. P. Thomas, M. W. Shi, D. Jayatilaka and M. A. Spackman, C*hem. Commun.,* 2015, 5**1,** 3735-3738.
11. R. F. Bader, C*hem. Rev.,* 1991, 9**1,** 893-928.
12. M. J. Frisch, G. W. Trucks, H. B. Schlegel, G. E. Scuseria, M. A. Robb, J. R. Cheeseman, G. Scalmani, V. Barone, G. A. Petersson, H. Nakatsuji, X. Li, M. Caricato, A. V. Marenich, J. Bloino, B. G. Janesko, R. Gomperts, B. Mennucci, H. P. Hratchian, J. V. Ortiz, A. F. Izmaylov, J. L. Sonnenberg, Williams, F.

Ding, F. Lipparini, F. Egidi, J. Goings, B. Peng, A. Petrone, T. Henderson, D. Ranasinghe, V. G. Zakrzewski, J. Gao, N. Rega, G. Zheng, W. Liang, M. Hada, M. Ehara, K. Toyota, R. Fukuda, J. Hasegawa, M. Ishida, T. Nakajima, Y. Honda, O. Kitao, H. Nakai, T. Vreven, K. Throssell, J. A. Montgomery Jr., J. E. Peralta, F. Ogliaro, M. J. Bearpark, J. J. Heyd, E. N. Brothers, K. N. Kudin, V. N. Staroverov, T. A. Keith, R. Kobayashi, J. Normand, K. Raghavachari, A. P. Rendell, J. C. Burant, S. S. Iyengar, J. Tomasi, M. Cossi, J. M. Millam, M. Klene, C. Adamo, R. Cammi, J. W. Ochterski, R. L. Martin, K. Morokuma, O. Farkas, J. B. Foresman and D. J. Fox, J*ournal,* 2016.

13. W. Humphrey, A. Dalke and K. Schulten, J*ournal of Molecular Graphics,* 1996, 1**4,** 33-38.
14. R. M. Parrish, L. A. Burns, D. G. A. Smith, A. C. Simmonett, A. E. DePrince, III, E. G. Hohenstein, U. Bozkaya, A. Y. Sokolov, R. Di Remigio, R. M. Richard, J. F. Gonthier, A. M. James, H. R. McAlexander, A. Kumar, M. Saitow, X. Wang, B. P. Pritchard, P. Verma, H. F. Schaefer, III, K. Patkowski, R. A. King, E. F. Valeev, F. A. Evangelista, J. M. Turney, T. D. Crawford and C. D. Sherrill, J*. Chem. Theory Comput.,* 2017, 1**3,** 3185-3197.
15. N. J. Hestand and F. C. Spano, J*. Chem. Phys.,* 2015, 1**43,** 244707.
16. F. Plasser and H. Lischka, J*. Chem. Theory Comput.,* 2012, 8**,** 2777-2789.
17. W. Q. Deng, L. Sun, J. D. Huang, S. Chai, S. H. Wen and K. L. Han, N*at Protoc,* 2015, 1**0,** 632-642.
18. F. Plasser, J*. Chem. Phys.,* 2020, 1**52,** 084108.